POLITECNICO
MILANO 1863

SCUOLA DI INGEGNERIA INDUSTRIALE
E DELL'INFORMAZIONE

Executive Summary of the Thesis

Pareto Optimization and Power Electronics Realization of Orthogonal Field WPT Concept

Laurea Magistrale in Electrical Engineering - Ingegneria Elettrica

Author: Devpriy Yadav

Advisor: Prof. Dr. Roberto Perini

Co-advisor: Prof. Dr. Johann Walter Kolar (PES, ETH Zurich)

Academic year: 2020-2021

1. Introduction

Modern Inductive Power Transfer (IPT) systems are in existence since 1960's where they found applications in biomedical and radio-frequency identification systems, mainly supplying implanted devices and for remote sensors.

In high purity industries such as pharmaceutical and semiconductor industries, the manufacturing environment have very high purity environment requirement. The manufacturing units are often enclosed in Stainless Steel enclosures to ensure high purity. To supply systems inside a closed environment is usually achieved by cable carriers. This may compromise the purity of the environment. Also with time, the cables loosens due to ageing which may also cause contamination. Thus transmitting power wirelessly is a promising solution. However, due to presence of conductive material in between the sending and receiving module, usually stainless steel (SS), there are losses in SS. This limits the maximum efficiency of the WPT module.

Previously an MSc thesis [8] has been conducted on this topic in which different wireless power transfer methods through SS has been studied and realized in hardware. The work included modelling the differnt WPT modules (OFC and PFC), analysing equivalent circuits and realizing and testing it in hardware demonstrator. The OFC-WPT module achieved 72% of maximum efficiency at 50W output power & 60V input voltage [6]. Figure 1 shows the OFC-WPT model developed along with it's performance parameters. This thesis extends the work to geometrically optimize the WPT module to increase efficiency, taking base design as in [6], and as shown in Figure 1b.

2. Fundamentals of Wireless Power Transfer & OFC-WPT

The main objective of ans IPT system is to transfer power to a moveable component across gapped magnetic structure. The complete realization of Inductively Coupled WPT system is an intricate amalgamation of magnetics and power electronics . Due to the large air gap, the magnetic coupling between primary and

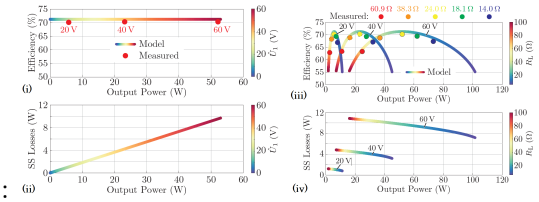

(a) Base Design Performance:: **(i)**: $Eff.$ vs P_{out} as a function of $\hat{U}_1$, shows constant trend of efficiency over entire voltage range, **(ii)**:$SS\ Losses$ vs P_{out} as a function of $\hat{U}_1$, shows linear trend, **(iii)**: $Eff.$ vs P_{out} as a function of R_L, **(iV)**: $SS\ Losses$ vs P_{out} as a function of R_L.

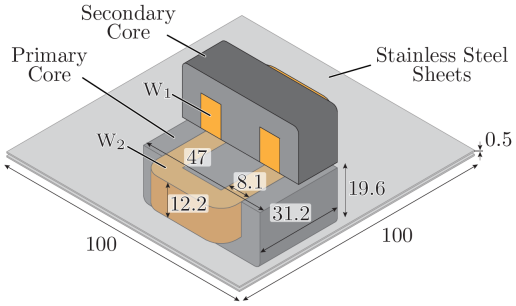

(b) Base Design (All dimensions in mm)

Figure 1: Previous Work on OFC-WPT [6]

secondary is lower, which leads to low mutual inductance and higher leakage inductance. Because of this, the power conditioner along with circuit tuning is required for efficient operation of WPT system. [1]

The basic principle of operation of WPT is governed by Amperé's law and Faraday's law. The working of ICWPT can be modelled and better understood by equivalent circuit of a transformer [3]. The analysis of MF transformers for Power Electronic applications can be split in various categories, such as [5]: *Magnetic, Electric, Losses, Thermal.*

The main element of a WPT system is the magnetics, as the energy transfer from primary side to the secondary side is achieved via alternating magnetic field, guided through a magnetic core. An ideal transformer can be represented by two mutually coupled coils, as shown in Figure 2, the leakage field and mutual field can be modelled by Leakage Inductance (L_σ) and Mutual Inductance (L_μ or M) respectively.

The two main types of WPT methods employed through SS are: **(a)**: Parallel Field WPT

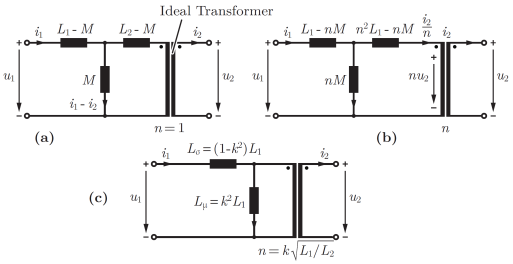

Figure 2: Equivalent circuit of an ideal transformer: **(a):** Ideal transformer with $n = 1$, **(b):** Ideal transformer with $n \neq 1$, **(c):** Ideal transformer with $n = k\sqrt{L_1/L_2}$; [3]

Concept (PFC-WPT), & **(b):** Orthogonal field WPT concept (OFC-WPT), depending on the way the magnetic field penetrates the SS. (ref. Figure 3).

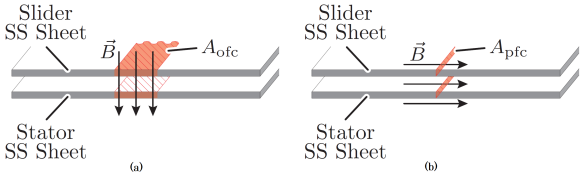

Figure 3: WPT Concepts through SS: **(a)**: Orthogonal Field Concept (OFC) - $\vec{B}$ & SS sheets are orthogonal, & **(b):** Parallel Field Concept (PFC) - $\vec{B}$ & SS sheets are parallel

The main focus of thesis is on OFC-WPT. The magnetic field lines cross SS sheets orthogonally. The WPT module is realized on a ferrite E-core srtucture, one for each: sending and receiving end. The module is supplied to the sending end winding via a DC-AC converter. This sets up the alternating magnetic field in the core which crosses the air gap, through the SS sheets, and closes through the receiving end module. This mutually coupled flux induces voltage in the secondary winding. The secondary side is connected to the load through a diode bridge.

The OFC-WPT is modelled as a 3-winding transformer [6] with SS sheet modelled as single turn, short-circuited winding. The equivalent circuit of the OFC-WPT is shown in Figure 4(b). KVL can be applied and equations can be written for the three windings, after simplification these can be written as shown in Equation set 1.

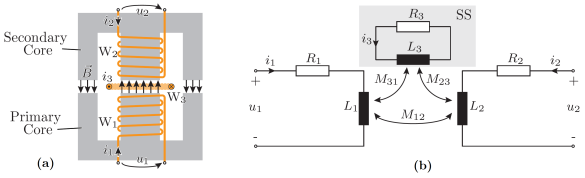

Figure 4: Equivalent circuit model of OFC-WPT

$$\begin{cases} u_1 = R_1 i_1 + (L_1 - M)\frac{\mathrm{d}i_1}{\mathrm{d}t} + M\frac{\mathrm{d}}{\mathrm{d}t}(i_1 + \frac{i_2}{n} + \frac{i_3}{m}), \\ nu_2 = n^2 R_2 \frac{i_2}{n} + (n^2 L_2 - M)\frac{\mathrm{d}\frac{i_2}{n}}{\mathrm{d}t} + M\frac{\mathrm{d}}{\mathrm{d}t}(i_1 + \frac{i_2}{n} + \frac{i_3}{m}), \\ 0 = m^2 R_3 \frac{i_3}{m} + (m^2 L_3 - M)\frac{\mathrm{d}\frac{i_3}{m}}{\mathrm{d}t} + M\frac{\mathrm{d}}{\mathrm{d}t}(i_1 + \frac{i_2}{n} + \frac{i_3}{m}). \end{cases} \quad (1)$$

Based on the equation set 1, the equations can be further simplified to reduce the equivalent circuit of OFC-WPT similar to an equivalent circuit of a real transformer having components: Leakage and Mutual Inductances ($L_s = N_t^2 \cdot L_{s0}$ & $M = N_t^2 \cdot M_0$), loss components ($winding: \ R_w = N_t^2 \cdot R_0$, $solid\ losses: \ R_{ss} = N_t^2 \cdot R_3$). These parameters of OFC-WPT are depicted in simplified equivalent circuit of OFC WPT shown in Figure 5, and can be obtained from Z-parameters as [6]:

$$\begin{aligned} R_0 &= \Re(\underline{Z}_{11} - \underline{Z}_{12}) \\ L_{s0} &= \Im(\underline{Z}_{11} - \underline{Z}_{12})/\omega, \\ M_0 &= 1/\Im(1/\underline{Z}_{12}^*) \cdot 1/\omega, \ \& \\ R_3 &= 1/\Re(1/\underline{Z}_{12}^*). \end{aligned} \quad (2)$$

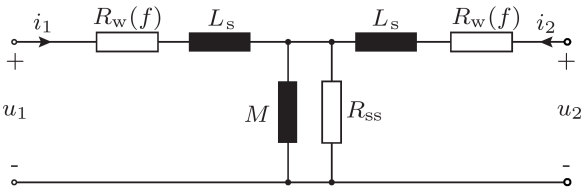

Figure 5: Complete equivalent circuit of OFC-WPT through SS

3. Model and Optimization Methods

As explained in Section 2, in OFC-WPT the magnetic flux passes from transmitter module inside the core, through the air gap and crosses the SS sheets and finally closing through the receiving module core. It can be evaluated using Amperé law that the induced EMF in SS sheets will be maximum in the air gap between the limbs of the core. Figure 6 shows the distribution of induced EMF as a function of distance along the center line of SS sheet.

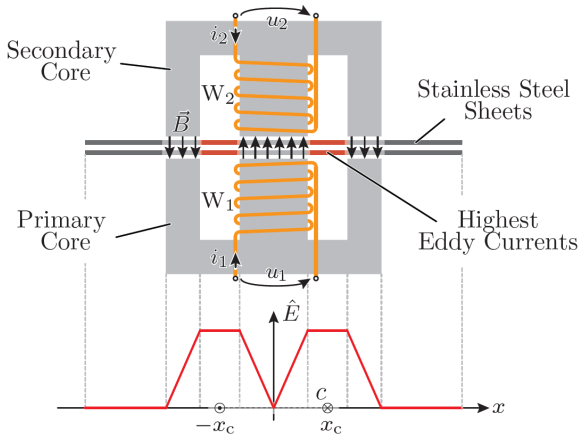

Figure 6: Induced EMF distribution for an E-core type OFC WPT module

This will cause the eddy current to flow in the SS sheets and thus, there will be losses associated with the SS sheets. Figure 7 shows the distribution of Eddy current density in the SS sheet. This loss component is reflected as an equivalent resistance R_3 in the equivalent circuit of the winding model of SS (see Figure 4). In the simplified equivalent circuit, this equivalent SS resistance is represented by R_{SS} (see Figure 5). The induced eddy current density distribution is shown in Figure 7

Proposed Modifications

Since R_{SS} contributes towards maximum reduction of losses in SS, increasing the value of R_{SS} would reduce loses in SS, and thus increasing the overall efficiency of the module. As seen in Figure 7, the current density is maximum in the slit between the core limbs, and thus it contributes maximum to R_{SS}, since the current spreads out in the SS sheet in the area outside the slit, thus, reducing the width of this slit may increase the R_{SS}. Figure 8 shows the proposed modifications.

To achieve this, Pole Shoes can be introduced at the ends of the limbs to reduce the overall width of the air-gap. This would in turn reduce

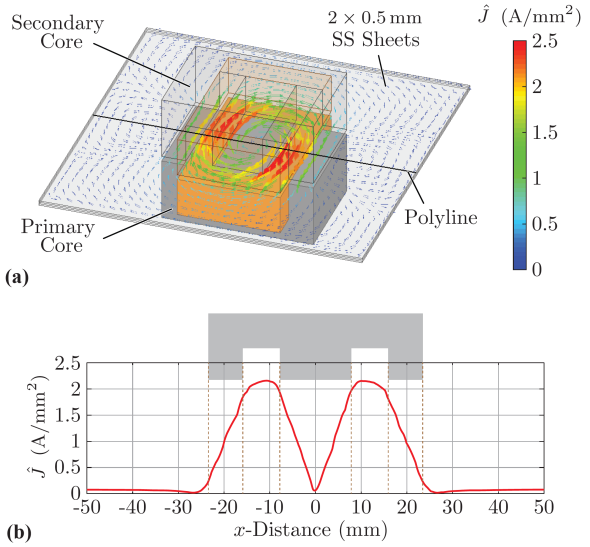

Figure 7: Induced Eddy Current distribution for an E-core type OFC WPT module along the center line of SS sheets.

the cross sectional area of the eddy current path and thus increasing R_{SS}. Different Pole shoe shapes were first analysed in the FEM environment to see which pole shoe placement is best (see Figure 8). From the results, it was found that Pole Shoes placed symmetrically inside the air-gap gives best results with symmetric magnetic field distribution (as shown in Figure 8(b)).

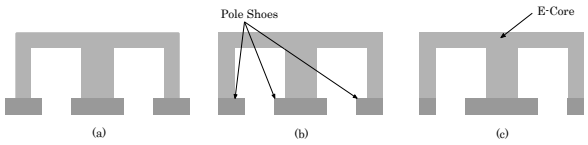

Figure 8: Pole Shoe Types explored:: **(a)**: Pole Shoes placed at the center of each limb with equal pole width on each side, **(b)**: Pole shoes placed symmetrically to get symmetric gap between the pole shoes, **(c)**: Pole shoes placed on central limb to increase distance between air-gaps.

The details of geometrical dimensions are shown in Figure 9. The description of various geometrical dimensions involved is given in Table 1

The main aim of this modification is to reduce the losses in the SS sheets. However, there are many other parameters which also affect the efficiency, for e.g. Switching Frequency (f_{sw}),

Table 1: **Description of Geometrical Dimensions**

l_c : Core length	h_c : Core height
w_c : Core width	t_c : Core limb thickness
w_w : Winding width	h_w : Winding height
l_w : Winding length	g_{ps} : Pole shoe gap
h_{ps} : Pole shoe height	A_c : Core Area ($t_c \cdot l_c$)
A_w : Winding window area ($h_w \cdot w_w$)	x_c : Core aspect ratio (l_c/t_c)
w_{ps} : Poles shoe width	

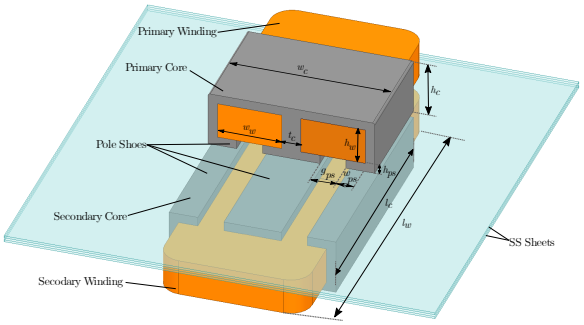

Figure 9: Geometrical Dimensions of OFC-WPT Module

No. of turns (N_t), Input Voltage ($\hat{U_{in}}$) etc.

To find the best performing parameters, we must perform an optimization routine. The output of this optimization should give the set of all the parameters (geometrical as well as operational) which would give us maximum efficiency for the module. In order to start optimization, the system needs to be modelled based on the analysis type as discussed in Section 2. There are various ways to obtain the full-model of a system for optimization, classified in three categories: *Numerical, Semi-Numerical, Analytical* [4]:

For the purpose of this thesis, FEM model and Fully - Analytical Models are used. Initially, the FEM approach was used to get the model parameters, and then optimization was run in MATLAB program. This optimization method was kept unconstrained and all the parameters were varied. This resulted in getting most optimum designs at the extremes of the design space. This approach was therefore not suitable, hence analytical model was developed and optimization was run with fully analytical model in MATLAB. The analytical method is discussed below.

Analytical Modelling & geometry optimization

The different circuit elements of OFC-WPT, namely R_w, L_s, M, & R_{SS} (Figure 5) needs to be modelled individually to analyse the performance of the module. These parameters are linked with geometrical as well as operational parameters. Thus, the analytical closed form equations needs to be developed which links the operational & geometrical parameters with the circuit parameters:

Magnetic Modelling of OFC-WPT module

The magnetic modelling of the E-core is to be done to determine the flux linkage of the transmitter module with the receiver module. The mutual flux linked with primary (transmitting side) and secondary (receiving side) mainly contributes to the power transfer. However, not all the flux that is generated in the primary module links with the secondary side. Some flux lines closes through the air within the primary (or secondary) modules, which is called the *Leakage Flux*.

The two flux fields: *Leakage & Mutual* fluxes can be modelled as Inductances, namely: *Leakage* (L_σ) *& Mutual* ($M or L_\mu$) Inductance respectively. Referring to the equivalent circuit of the OFC-WPT (Figure 5), the primary and secondary sides have their respective leakage inductances (L_σ). The mutual inductance (M) takes into account the flux linked with Primary & Secondary and also the flux linked with SS sheets.

The megnetic circuit modelling of the WPT is analogous to modelling electric circuit. Just like KVL for electric circuits, the Amperé's Law states that sum of magnetomotive force (MMF) in a closed loop is zero and similar to KCL, the Gauss' law for magnetic circuit states that sum of magnetic flux at a node is zero. Similar to resistance in electric circuits, the resistance of flow of magnetic flux in defined as *Reluctance*: $R_m = MMF/\phi$. Hence the magnetic model is also simply called the *Reluctance Model*. [7]

Using the reluctance model, the inductance of any inductive components having N_t turns of winding and total reluctance $R_{m,tot}$ can be evaluated as:

$$L = \frac{N_t^2}{R_{m,tot}} \tag{3}$$

To get the indutance, we must first know the reluctance of each section of the inductive component. The OFC-WPT module thus can be divided into different sections as shown in Figure 10(a). For each section, the reluctance can be calculated as:

$$R_m = \frac{l}{\mu_0 \mu_r A_{cm}} \tag{4}$$

where R_m is the reluctance of the path/section, l is the length of the section, A_{cm} is the cross sectional area of the magnetic material section and $\mu_0\mu_r$ is the permeability of the section ($\mu_r = 1$ for air). [7]

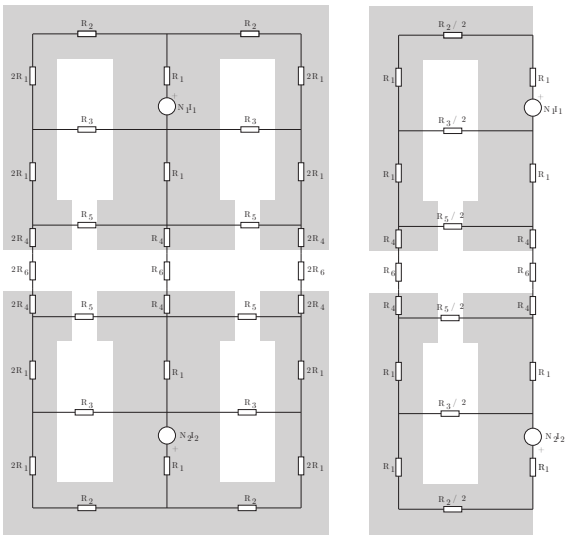

(a) (b)

Figure 10: Magnetic modelling of OFC-WPT module:: **(a)**: E-core split into different sections and reluctances calculated for for each section, **(b)**: Reluctance model simplified along the central symmetry axis.

Referring to Figure 10(a), the reluctances R_1, R_2 & R_4 are the reluctances of the magnetic material, while reluctances R_3, R_5 & R_6 are reluctances in the air path. The reluctance

R_3 & R_5 contributes to the leakage inductances.

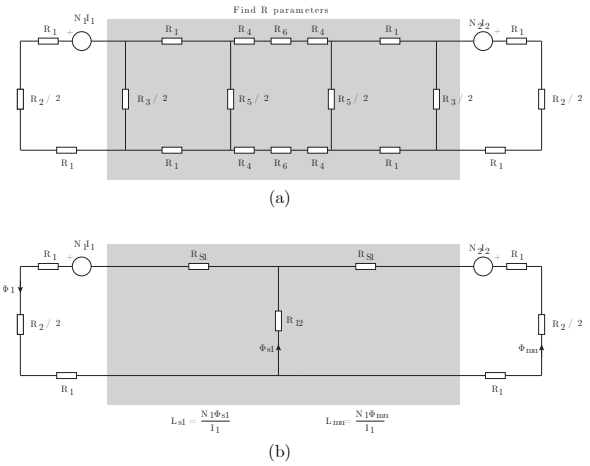

Figure 11: Reluctance network of OFC-WPT module:: **(a)**: Reluctance network of simplified magnetic network (Figure 10(b)). The network in the shaded area is a typical ladder network, **(b)**: The ladder network is reduced to T-network.

Using symmetry, the reluctance network shown in Figure 10(a) can be simpified to that shown in Figure 10(b) & Figure 11(a). This is a typical ladder network which can be reduced to an equivalent-T network as shown in Figure 11(b). From this, the total flux ϕ_1 can be split into the mutual flux ϕ_m and leakage flux ϕ_{s1}. Using this, we can calculate the inductances as:

$$Ls1 = \frac{N_1\phi_{s1}}{I_1} \quad \& \quad L_{mu} = \frac{N_1\phi_{mu}}{I_1} \tag{5}$$

SS Resistance Calculation

As discussed in previously, the alternating flux generated by exciting the primary winding, crosses the SS sheets orthogonally in OFC-WPT. This alternating flux induces eddy currents in the SS sheets and contributes to solid losses. These losses can be modelled as an equivalent resistance R_{SS} as shown in the equivalent circuit of OFC-WPT (Figure 5). From the Equations 1, we can see that R_{SS} can be written as:

$$R_{SS} = N_t^2 \cdot R_3 \tag{6}$$

where N_t is the number of winding turns and R_3 is the single turn SS resistance. Since N_t is known quantity, we need to model R_3 to get the value of R_{SS}.

We had already seen previously that the induced eddy currents mainly flows in the slit between the core limbs. This can be seen clearly in Figure 12 that this portion of SS (R_1) contributes mainly towards the total resistance in R_3, as the eddy currents can spread in wider area outside this region and thus the resistance of this region (R_2) in quite lower as compared to the section of SS directly below the slit. Moreover, it is quite difficult to estimate the total resistance in the region outside the slit, so empirical methods are used to correct for the resistance value.

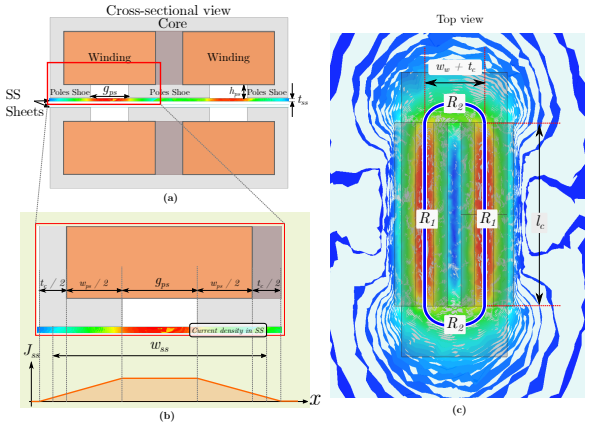

Figure 12: SS Resistance calculation

We had seen previously (Figure 7) that the current density is maximum in the slit area and has more of a trapezoidal distribution (ref. Figure 12). Thus, for our analysis, we can approximate a trapezoidal cross-section of SS sheet directly below the slit region for calculation of SS resistance in this region. Figure 12(b) & 12(c) shows the current density distribution approximation and the dimensions involved.

The effective width of the SS sheet therefore can be approximated as shown in Figure 12(b). Therefore, for the region below the slit, the SS resistance R_1 can be approximated as given in Equation 7:

$$\begin{cases} w_{ss} = g_{ps} + w_{ps} + \dfrac{t_c}{2} \\ l_1 = l_c \\ A_{ss} = t_{ss} \cdot w_{ss} \\ R_1 = \dfrac{l_1}{\sigma_{ss}\ A_{ss}} \end{cases} \tag{7}$$

where σ_{ss} is the conductivity of the SS, w_{ss} is the effective cross-sectional SS width, t_{ss} is the SS sheet thickness (0.5 mm thick SS sheets are used) and A_{ss} is the effective cross sectional area of the SS sheets for R_{SS} calculation.

For the region outside the slit, it is quite difficult to accurately calculate the path length taken by eddy currents. This path length can be approximated by arc from one side to other as shown in Figure 12. Moreover, the analytical model was verified in FEM an iteratively, a correction factor was used to match closely the value of R_{SS} from analytical calculations with the FEM based results. A closed form empirical result for R_2 is obtained as in Equation 8:

$$\begin{cases} l_2 = 1.5 \cdot (w_w + t_c) \\ R_2 = \dfrac{l_2}{\sigma_{ss}\ A_{ss}} \end{cases} \tag{8}$$

Finally R_3 & hence R_{SS} can be calculated as in Equation 9:

$$\begin{cases} R_3 = 2 \cdot (R_1 + R_2) \\ R_{SS} = N_t^2 \cdot R_3 \end{cases} \tag{9}$$

The analytic model developed to calculate SS resistance however calculates the DC resistance and frequency dependent effects are neglected.

Frequency dependent AC winding resistance modeling

The conduction losses in the winding of OFC-WPT are modelled as equivalent winding resistance. The DC resistance of the windings can be straightforward calculated from the geometrical dimensions and winding material properties (Cu) as:

$$R_{w0,DC} = \frac{l_{Cu}}{\sigma_{Cu}\ A_w} \tag{10}$$

where $R_{w0,DC}$ is the single turn DC winding resistance, σ_{Cu} is the conductivity of the copper, $l_{Cu} = 2(2w_w + 2l_c + t_c)$ is the effective copper turn length, and A_w is the winding window area.

The total winding resistance for a N_t turn winding can be obtained as:

$$R_{w,DC} = N_t^2 \cdot R_{w0,DC} \tag{11}$$

However, for accurate calculation of Cu-losses, the high frequency effects needs to be considered. The two main HF effects namely: *Skin & Proximity* effects needs to be modelled to get the total AC losses. Thus, the AC resistance of the winding can be split into two components: $R_{w,AC-skin}$ & $R_{w,AC-proximity}$. The calculation method of these are well established in the literature and in this thesis, one such method is used as described in [2] is used:

$$\begin{cases} R_{w,AC-skin} = R_{w,DC} \cdot 2F_R \\ R_{w,AC-prox} = R_{w,DC} \cdot 2G_R \cdot \left(\dfrac{H_{ext,RMS}}{I_{RMS}}\right)^2 \\ R_{w,AC} = R_{w,AC-skin} + R_{w,AC-prox} \end{cases} \tag{12}$$

The constants F_R & G_R depends mainly on geometrical parameters of winding and frequency and can be evaluated easily from the closed form expressions. The main issue in calculating proximity effect comes to calculate the H-field distribution in the winding. The contribution of skin and proximity effect for each winding turn needs to be calculated individually and all the contributions needs to be added finally to get the final AC resistance. For this, the H-field at each winding turn needs to be evaluated.

In FEM method, the H-field inside the volume of winding can be exported and interpolated at the centers of wires to calculate contribution towards proximity effect for each turn.

In analytical method, the winding turns are assumed to be arranged in a rectangular fashion as shown in Figure 13 and $1A$ current is assumed to be flowing. Amperé's Law can be used to calculate the H-field. Since the primary and secondary windings are not on the same core, the Amperé's law is used in two directions and H-field is calculated for each layer. The individual contribution of the H-field for each turn is vectorially added so we can evaluate the AC proximity resistance.

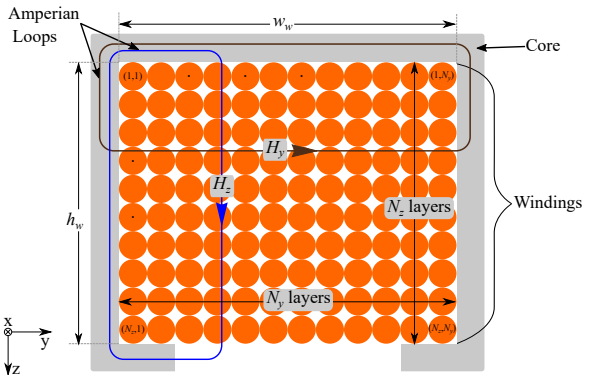

Figure 13: Analytical method of calculating H-field

For each layer in z and y direction, we can apply Apmperé's law. The H-field inside the magnetic material is zero and thus H-field exists only in the region of winding. Thus, H-filed in as z and y can be calculated as:

$$\begin{cases} (H_y)_{n_y} = \dfrac{N_t \cdot I_{rms}}{w_w} \cdot \dfrac{n_y}{N_y} \\ (H_z)_{n_z} = \dfrac{N_t \cdot I_{rms}}{h_w} \cdot \dfrac{n_z}{N_z} \end{cases} \tag{13}$$

where n_z is the layer number in z-direction, and it takes the values from $\{1\ to\ N_z\}$, n_y is the layer number in y-direction, and it takes the values from $\{1\ to\ N_y\}$. For each conductor at position (n_z, n_y), the H-filed can be calculated as:

$$H_{zy} = \sqrt{H_z^2 + H_y^2} \tag{14}$$

Geometrical Optimization

The main aim for optimization is to find the best parameters which would give the most optimum performance. This thesis mainly focuses on the geometry optimization of OFC-WPT to achieve best efficiencies. However, as we have seen previously that there are two many parameters involved, it is very difficult to interpret the pareto results. Thus, boxed volume optimization approach is used. Figure 14 shows the concept of boxed volume optimization.

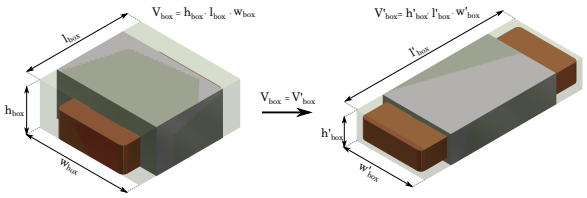

Figure 14: Box Optimization: The boxed volume of inductor is constant, while other geometrical parameters are varied.

The overall boxed volume of the inductor (including core and winding) is kept constant and the other geometrical parameters are varied. In addition to keeping the box volume constant, the output power and input voltage is also kept constant. Thus the module is optimized for constant 50W output power at fixed 60V input voltage. The optimization variables are therefore:

- Operational parameters: f_{sw}, R_{Load}
- Constructional parameters: N_t
- Geometrical Parameters (l_c, w_c, t_c, h_c, g_{ps}, ...)

For the purpose of optimization, the analytical approach is used. To keep the power constant at 50W, the load resistance needs to be calculated according to the circuit parameters. Once model parameters are calculated, the network is simplified to a Thevenin's Equivalent and for a constant 50W, the load resistance R_{Load} is calculated. Some optimization contraints are kept to filter out the invalid design. These are:

- Peak Flux density inside the core $\leq 0.3\ T$ (typical value for ferrite cores)
- Wire diameter $\leq 1\ mm$ (for easy winding on coil former)

Since the volume and output power are kept constant, the power density is therfore constant. Therefore, the $\eta - \rho$ pareto plot would be just

a straight line. Therefore, it is not a very convinient way to interpret the optimization results. Thus, the optimization results are plotted on a parallel-coordinate plot as shown in Figure 15 & 16. The base design is added along with all the other valid design in Figure 15 for comparison with the base design. Figure 16 shows all the valid design without the base designs.

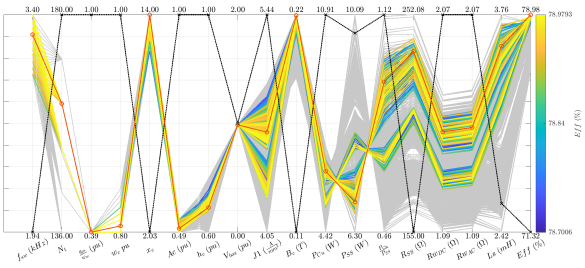

Figure 15: Parallel coordinate plot with base design included. The base design is highlighted in black, while chosen design is highlighted in orange. Designs not meeting filtering criteria are greyed out

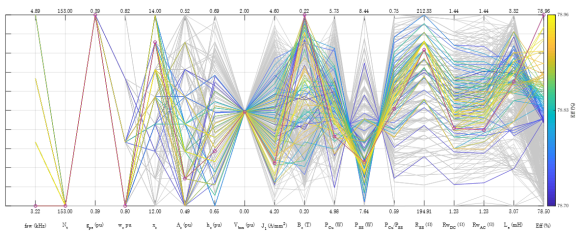

Figure 16: Parallel coordinate plot without base design included. The chosen design is highlighted in Blue. The invalid designs are greyed out.

4. Hardware Implementation and Results

Based on optimization results, we chose the highest efficiency design. The optimized design geometry with optimized geometrical dimensions is shown in Figure 17. The module is expected to operate of 78.9% efficiency. The analytical calculations of the module are verified by modelling it in FEM environment.

To realize the optimized design module, a custom made ferrite E-core was required. However, it was quite expensive to manufacture, hence

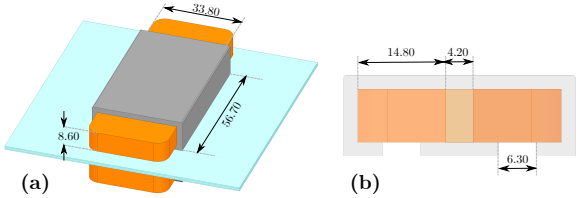

Figure 17: Physical dimensions of the optimized design:: **(b)**: 3D view, **(b)**: Cross-sectional view. (All dimensions are in *mm*).

the model was realized with small ferrite I-cores as building blocks.

The main E-core is assembled on a 3D-printed structure and the I-core are glued together to make the main E-core structure except the central limb. The central limb is inserted in the coild former and the winding and coil former is inserted in E-core structure to complete the E-core module.

The pole shoes are glued to the bottom of coil former to complete the assembly.

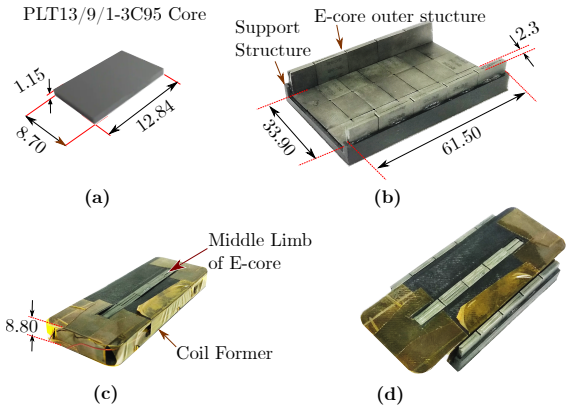

Figure 18: Actual assembly of OFC-WPT:: **(a)**: I-core, **(b)**: Outer structure of E-core glued on a 3D printed support structure, **(c)**: Winding wound on a 3D printed coil former and middle limb of E-core inserted in the slot, **(d)**: Coil shown in **(c)** is inserted in the E-structure shown in **(b)**. Finally pole shoes are glued to the bottom of coil former to complete the assembly. *(All dimensions are in mm)*

The WPT module is to be supplied by a Power Electronic converter system. Most common topology used for IPT applications is isolated DC-DC converters [3], Figure 19 shows the topology of a typical isolated DC-DC converter

system applied to IPT systems. The primary side is supplied through a $1-\phi$ inverter while the receiving side is a diode bridge.

The Primary side converter was realized using two Half bridges in H-bridge configurations. Existing MALTA board was used to realize the converter system. TI F28069M board was utilized to generate the PWM signals. Figure 20 shows the realized converter on PCB.

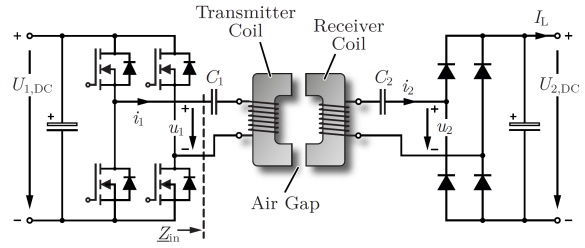

Figure 19: PE-converter topology for WPT applications [3]

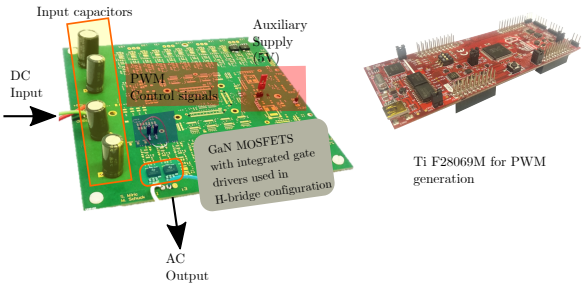

Figure 20: PE-converter for OFC-WPT

The WPT module realized is tested to observe the performance. Figure 21 shows the Impedance data obtained from a SC and OC measurement made on the realized WPT module:

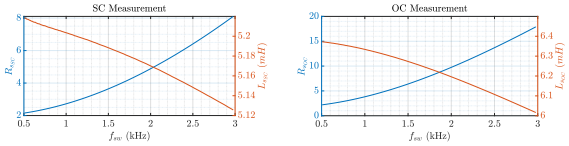

Figure 21: SC and OC measurement from Impedance Analyzer

Based on the Obtained SC and OC data, we can calculate the parameters. The plots of calculated parameters are shown in Figure 22:

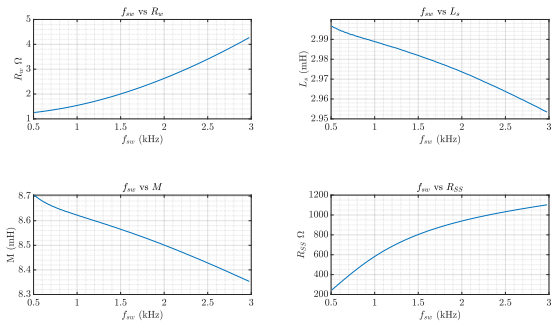

Figure 22: Circuit parameters of OFC-WPT module calculated from Impedance Analyzer measurement.

Based on the circuit parameters calculated from Impedance measurements, the performance of the OFC-WPT was evaluated. The performance trend can be sen in Figure 23. It can be seen that the efficiency of the module has increased from 72 % upto 84%.

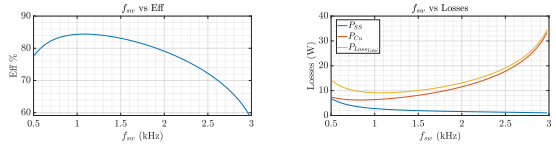

Figure 23: Efficiency and Loss plots for the OFC-WPT measurement data. The model has achieved an efficiency of $\approx$ 84 % while reducing the losses in SS as well as copper.

5. Conclusions

The effect of different geometrical parameter was observed on the circuit parameters, such as on SS resistance (R_{SS}), winding resistance (R_w), Leakage and Mutual inductances (L_σ & M), and on performance parameters such as N_t, f_{sw}, power losses, coupling factors etc. These observations were used to further refine the course of optimization.

The optimization resulted in a OFC-WPT module giving us $\approx$ 84% efficiency for same volume and input voltage. The optimized geometrical parameters allowed us to increase the R_{SS} from 155 Ω in base design to 635 Ω and hence reducing P_{SS} to 3W, reduce R_w from 2 Ω to 1.6 Ω hence reducing P_{Cu} to 6W and reducing total losses to 9W. The optimized

desgin is also operated at higher frequencies and with lower core cross sectional area, hence operating it near the knee on magnetic curve, thus utilizing the magnetic material better.

Finally the optimized design was developed in hardware and the results were verified by testing and measurements.

6. Acknowledgements

I would like to thank Prof. Dr. Roberto Perini for supporting me during my exchange period and also acting as supervisor at PoliMi. I would also like to extend my sincere thanks to Prof. Dr. Johann W. Kolar for giving the opportunity to be at PES lab, ETH Zürich and work on my MSc thesis as an exchange student. This experience would not have been possible without continuous support and supervision of Dr. Spasoje Mirić, who always helped whenever I was in doubt. He had always provided necessary resources necessary to complete the thesis. It would also not have been possible to be at PES without the support of Dr. Jonas Huber who gave me the opportunity work on this topic.I would also like to the exchange office of Politecnico di Milano and ETH Zürich for ensuring a smooth stay throughout. Finally, I would like to thank my family for always keeping my motivation high, and to my friends and colleagues for believing in me and keeping my spirit alive.

References

[1] Ali Abdolkhani. Fundamentals of inductively coupled wireless power transfer systems. In Eugen Coca, editor, *Wireless Power Transfer*, chapter 1. IntechOpen, Rijeka, 2016.

[2] Jürgen Biela. *Optimierung des elektromagnetisch integrierten Serien-Parallel Resonanzkonverters mit eingeprägtem Ausgangsstrom.* PhD thesis, ETH Zürich, 2005.

[3] Roman Bosshard. *Multi-Objective Optimization of Inductive Power Transfer Systems for EV Charging.* PhD thesis, ETH Zürich, 2015.

[4] Thomas Guillod and Johann Walter Kolar. Medium-frequency transformer scaling laws: Derivation, verification, and critical analysis. *CPSS Transactions on Power Electronics and Applications*, 5(1):18–33, 2020.

[5] Thomas Guillod, Florian Krismer, and Johann W Kolar. Magnetic equivalent circuit of mf transformers: modeling and parameter uncertainties. *Electrical Engineering*, 100(4):2261–2275, 2018.

[6] Spasoje Mirić, Mina Tatić, Jonas Huber, Dominik Bortis, and Johann W. Kolar. 'pushing power through walls" - wireless power transfer through stainless steel. In *2021 24th International Conference on Electrical Machines and Systems (ICEMS)*, pages 743–751, 2021.

[7] JONAS Mühlethaler. *Modelling and Multi-Objective Optimization of Inductive Power Components.* PhD thesis, ETH Zürich, 2012.

[8] Mina Tatić. Wireless power transfer through stainless steel. Master's thesis, ETH Zürich, 11 2021.